Fiber Bragg grating–differential settlement measurement system for bridge displacement monitoring

M. Bonopera[1,4*], K.-C. Chang[2], C.-C. Chen[1], Z.-K. Lee[1], Y.-C. Sung[1,3], N. Tullini[4]

[1]*Bridge Engineering Division, National Center for Research on Earthquake Engineering, Taipei, Taiwan*
No. 200, Sec. 3, Xinhai Road, Taipei, 10668, Taiwan

[2]*Department of Civil Engineering, National Taiwan University, Taipei, Taiwan*
No. 1, Sec. 4, Roosevelt Road, Taipei, 10617, Taiwan

[3]*Department of Civil Engineering, National Taipei University of Technology, Taipei, Taiwan*
No. 1, Sec. 3, Zhongxiao E. Road, Taipei, 10608, Taiwan

[4]*Department of Engineering, University of Ferrara, Ferrara, Italy*
No. 1, Via Saragat, Block A, Ferrara, 44122, Italy

*Corresponding author - Emails: bonopera@ncree.narl.org.tw - marco.bonopera@unife.it

Abstract: Vertical displacements are one of the crucial parameters defining, for example, the load–carrying capacity of a bridge deck in short and long terms monitoring. Bridge managers are always looking for an easy way to measure vertical displacements of bridges. However, such measurements are difficult to perform. With the advancement of fiber–optic technologies, Fiber Bragg Grating (FBG) sensors are more commonly used in structural health monitoring due to their outstanding advantages including multiplexing capability as well as high resolution and accuracy. In this study, FBG–Differential Settlement Measurement (DSM) sensors, connected by hydrostatic leveling system of communicating vessels, were used for the displacement measurements along a large–scale Prestressed Concrete I (PCI) beam. Specifically, the member was subjected to a set of three–point bending tests in the laboratory. The measured displacements matched well with the corresponding experimental values using Linear Variable Differential Transformers (LVDT). In addition, *in situ* experiments on Bridge No. 24 of Highway No. 86 in Taiwan indicated that FBG–DSM system can be effectively employed to measure vertical displacements along span bridges. In conclusion, the proposed FBG–DSM system can be applied referring to an absolute reference and

without any external physical reference.

Keywords: Bridge; Deflected shape; Vertical displacement; FBG–DSM system; Optical fiber.

Introduction

Knowledge of the vertical displacement field of a bridge is crucial for assessing the structure's safety (Aldar 2013). Direct measurement techniques such as using dial indicators (Bonopera et al. 2018a), Linear Variable Differential Transformers (LVDTs) or transducers (Skelton and Richardson 2006) require fixed references at the measurement points, which are difficult to apply in practice. Vice versa, the accuracy of traditional geodetic or digital image processing techniques (Lee and Shinozuka 2006) is generally limited by displacement errors of at least one millimeter. Additionally, the aforementioned systems are completely unsuitable for long term measurements. To overcome these difficult tasks, Guan et al. (2019) have developed a specific smart radar sensor network for bridge displacement monitoring. The hydrostatic leveling system comprises communicating vessels filled with an appropriate liquid fixed to the structure at selected points. As a rule regarding fixed supports, one vessel of the circuit is designated as the datum reference and without any external physical reference. The constant absolute altitude of the liquid–free surface is ensured by the hydrostatic equilibrium of the communicating vessels. Consequently, vertical displacements can be obtained by measuring the liquid height variation in each vessel. Typically, a resolution of few tenths of a millimeter can be obtained. Sensors proposed for practical application differ in terms of how the liquid level is measured (Marecos 1978, Vurpillot et al. 1998, International Federation for Structural Concrete 2003, Rodrigues et al. 2010, Rodrigues et al. 2011, Dai et al. 2012). Specifically, in Rodrigues et al. (2010, 2011), Fiber Bragg Grating (FBG)–based sensors connected to a float on the liquid were used as transducer load cells to measure the apparent immersed weight of a suspended float, which is a linear function of the liquid level inside the sensor. The FBG–Differential Settlement Measurement (DSM) sensor, used in this study, employs prestressed clamped FBG with a direct connection to the immersed float, as illustrated in Bonopera et al. (2018b). Lai et al. (2016) used the same FBG mechanism for liquid–level sensors to conduct railway track differential settlement measurements. By contrast, Consales et al. (2018) studied such a sensor for accurate liquid level monitoring in large–scale storage tanks. The performance calibration tests for vertical displacements using the FBG–DSM sensors are currently limited. Only preliminary field measurements were executed on bridges (Chang et al. 2012, Lee 2013, Lee et al. 2014). Generally, the mechanism of the FBG–DSM system can furnish accurate measurements. Notably, some nondestructive methods based on vertical displacements were developed for axial force identification in beams (Tullini et al. 2012, Tullini 2013, Bonopera et al. 2018b, 2018c) and for prestress force prediction in concrete members (Bonopera et al. 2018d). In Bonopera et al. (2018b), a FBG–DSM system, similar to that used in this study, was employed for the axial load detection in a compressed steel beam by several laboratory measures.

In this paper, a FBG–DSM liquid–level system is proposed for differential settlement measurements along span bridges, referring to an absolute reference and without any external physical reference to the ground. Essentially, FBG possesses the advantages of electrical passivity, corrosion resistant and superior multiplexing capabilities over long distances. These features render FBG a good alternative sensing element for displacement measurements. First, a large–scale Prestressed Concrete I (PCI) beam was adopted in laboratory testing to simulate a typical bridge member. Three–point bending tests with different prestress forces were performed to involve various deflected shapes to the beam. A series of FBG–DSM sensors, connected by hydrostatic leveling system of communicating vessels, measured the vertical displacements at given cross sections along the member axis. Reliability of the sensors was evaluated by comparing their measurements from 36 three–point bending tests with recorded displacements by Linear Variable Differential Transformers (LVDTs) located at the same cross sections. Second, a monitoring system was deployed along Bridge No. 24 belonging to the Highway No. 86 in Taiwan. In this case, reliability of the FBG–DSM sensors was estimated by comparing their measurements with displacements recorded by dial indicators. Results indicated that the proposed FBG–DSM system can be effectively applied to measure vertical displacements along span bridges.

FBG–DSM system

Optical fibers are a transmission medium of light energy or signals. These intrinsic fiber sensors are based on the optical properties of processed or unprocessed fibers such as Brillouin sensors, Raman sensors, and evanescent sensors. In this study, intrinsic optical fibers exposed to artificial ultraviolet irradiation were used to form FBGs by employing phase masks with the corresponding reflected central wavelength of the FBGs. Variations in stress (strain) and temperature engender changes in the central wavelength of FBGs, which can be analyzed using a signal–processing device to convert the reflected signals. Hence, FBGs are sensing components and have sensing functionality. Through a mechanical procedure, FBGs can be used to designate sensing devices such as displacement or strain sensors (Kim and Cho 2004) for different purposes. For example, Kim et al. (2011) and Sung et al. (2017) have designed FBG sensors embedded in prestressing tendons to measure the applied tension force and load transfer along a tendon's length.

The key method proposed by the National Center for Research on Earthquake Engineering (NCREE) is to clamp the optical fiber with heat shrinkable sleeves for a total length of 100 mm, expressed as "S1+FBG+S2" in Fig. 1, which are used as connectors between the bare fiber and additional element to introduce external forces into the FBG. This design enhances the stability of the internal component of the FBG–DSM sensor. Thus, instrument components can exert prestress, which serves as the sensing origin (Fig. 1). Specifically, the FBG–DSM sensor comprises a suspended mass, FBGs, and two sleeves. One sleeve is directly connected to the suspended float mass and the other one is connected to the upper fixed end of the customized container, as shown in Fig. 2. The layout of the FBG–DSM sensing system is illustrated in Fig. 3; the communicating vessels contain a homogeneous fluid and the elastic range of FBGs is governed by floating mechanics and Hooke's law. According to the buoyancy principle, the magnitude of the buoyancy force is equal to the weight of an equal volume of fluid. Therefore, as the immersed volume of the suspended object increases, the force detected by FBG from pulling the suspended object changes. In detail, the maximum prestress force of the fiber is equal to the weight of the suspended float mass minus half of the volume of the floating body multiplied by the water density. Changes in water surface height do not affect the overcoming of the ultimate tensile strength of the optical fiber. The main properties of the fiber in the FBG–DSM sensors employed in this study are shown in Table 1.

Several FBG–DSM sensors can be linked using a connecting pipe. When a FBG–DSM sensor displaces downward with the beam span under monitoring, the suspended internal cylindrical object (with higher density than the liquid) also moves downward. However, its liquid surface moves relatively upward inside the sensor until the same liquid surface has been obtained within the connected FBG–DSM sensors. Therefore, variations in the buoyancy of the floats modify the force exerted on the FBG, thereby changing the reflective light wavelength. With respect to the linear behavior of the FBG material, the mathematical expression for the FBG–DSM sensor can be expressed as follows:

$$\begin{aligned}&\Delta\left(liquid\ surface\ height\right) \propto \Delta(buoyancy) \propto \Delta(fiber\ stress) \propto \\ &\propto \Delta(fiber\ strain) \propto \Delta(central\ wavelength\ of\ the\ reflective\ light).\end{aligned} \tag{1}$$

The data logger can be located on the ground, whereas the optical wires run externally and internally through the FBG–DSM sensors. Once the logger instrument has measured the Δ (*central wavelength of the reflective light*), the Δ (*liquid surface height*) can be obtained (Eq. (1)), thereby enabling the corresponding vertical displacement to be obtained. In short, the FBG–DSM sensor can furnish settlement measurements from the change in wavelength of the fiber within the container. In fact, the liquid height variation of the water into the vessel produces a difference in the wavelength of the installed fiber. A numerical example of one displacement measurement is described in Bonopera et al. (2018b).

The maximum stroke of the employed FBG–DSM sensor was 180 mm. A linear variation in the wavelength was observed because of the internal dimensions of the suspended cylindrical object of 38.5 mm–diameter and customized volume of the packaging case of the FBG–DSM sensor. When the maximum stroke of 180 mm is reached, the elongation of the used acrylic fiber is of approximately 0.103 mm with a wavelength shift of 3.04 nm (Table 1). The ultimate elongation of the used fiber corresponding to its ultimate tensile strength is of approximately 0.20 mm, corresponding to a wavelength shift of approximately 6 nm (value obtained from tensile test on the fiber) (Table 1). Notably, the FBG deformation (tensile elongation) does not represent the settlement of the FBG–DSM sensor. Even if the water flows beneath the bottom surface of the suspended internal float mass, the fiber does not reach the ultimate tensile strength.

Every conventional electronic sensor such as dial indicator or LVDT requires individual wire connected to the data logger or remote transmission module. Therefore, complicated wire connections are usually required when numerous sensors are applied (Ozdagli et al. 2017). One of the advantages of optical sensing technology is the plain connection of the sensors enabled by FBGs with different reflection wavelengths connected in series by a single transmission optical fiber. Figure 3 shows a set of FBG–DSM sensors; additional sensors can be linked in one channel depending on the wavelength band of the instrument's input light as well as splice fusion for the optical fiber. More details are furnished in the literature review by Bonopera et al. (2018b), and in preliminary field bridge testing (Chang et al. 2012, Lee 2013, Lee et al. 2014).

Calibration testing for the measured displacements by the FBG–DSM system

The FBG–DSM sensor used in this study can provide vertical displacements with 0.1 mm–tolerance. Thirty–six three–point bending tests were performed on a large–scale PCI beam (see

Section “PCI beam with a straight unbonded tendon and related test layout”) to verify the accuracy of numerous measured displacements by the FBG–DSM system. Specifically, a calibration of the aforementioned measurements was conducted by LVDTs, of 0.01 mm–tolerance, positioned at the same cross sections of the FBG–DSM sensors. In all test combinations, no relaxation occurred in the FBGs inside the sensors because the prestress force magnitudes (in the fiber) were moderate. Corresponding to the maximum measured displacement of v_3 = 14.0 mm (Table 2), the tensile elongation of the fiber was of approximately 0.008 mm, which was considerably lower than its ultimate tensile elongation of approximately 0.20 mm (Table 1). No FBG–DSM sensors were used for temperature compensation because the temperature in the indoor laboratory was reasonably assumed to be homogenous. The effect of temperature variation on wavelength changes in the FBG–DSM sensors was constant. Therefore, wavelength changes among the FBG–DSM sensors were only caused by the vertical displacements (deformations) of the PCI beam.

PCI beam with a straight unbonded tendon and related test layout

A large–scale PCI beam of b = 450 mm in width and h = 900 mm in height was adopted (Fig. 4). The beam was longitudinally reinforced with rebars and transversally with stirrups, in accordance with the Building Code Requirements for Structural Concrete (ACI 318–14). The straight unbonded tendon had an eccentricity of e = 220 mm (e / h = 0.24) with respect to the centroid of the cross section. The tendon was composed by 15 steel cables “seven wire strand” of 15.2 mm–diameter inserted into a metallic duct embedded along the PCI beam’s length (Fig. 4). Two pinned–end supports were positioned at the beam ends to reproduce the most common boundary conditions of bridge beams, resulting in a clear span of L = 14.5 m (Fig. 4). The cross sectional area of the straight tendon A_{tendon} was 2.085 × 10^3 mm^2. The cross sectional second moment of the area for the PCI beam composite section, concrete and cable, I_{exact} was 2.696 × 10^{10} mm^4. The slenderness ratio was equal to 49. The beam had a rectangular cross section of b × h = 450 mm × 900 mm for a length of 650 mm from the pinned–end supports.

The PCI beam was inserted in a test rig (Fig. 5(a)). At one beam end, a hydraulic oil jack of 4000 kN–force capacity was used to apply a prestress force to pull the strand outward. At both ends, respectively, a 4000 kN load cell with 2 mV/V accuracy was placed to measure the assigned prestress forces N_{0x1} and N_{0x2} (Fig. 5(b)). In total, four prestress forces $N_{0x,aver}$ were applied by values of approximately 1565, 1722, 1819 and 1920 kN to prevent cracking phenomena and induce small second–order effects, as typical of PCI beams (Bonopera et al. 2018e), equal to 3.4%, 3.8%, 4.0% and 4.3% of the Euler buckling load N_{crE}, respectively. A difference of approximately 100 kN between the prestress forces $N_{0x,aver}$ was firstly planned. The safety conditions of the laboratory involved the higher prestress force ($N_{0x,aver}$ = 1920 kN) to be lower than 2000 kN. Thus, the maximum tensile strength, reached in the tendon, was of approximately 50% of the ultimate yield strength of the cables. The different prestress forces N_{0x1} and N_{0x2} were caused by the friction losses along the tendon (Fig. 4). For every assigned prestress force $N_{0x,aver}$, a vertical load F was applied by a transverse steel beam at the PCI beam's midspan (Fig. 5(c)). The load F was increased from its initial magnitude, then gradually to two different values, depending on the magnitude of the prestress force $N_{0x,aver}$ (Table 2). The load F was always pulled both up and down using two hydraulic oil jacks, of 1000 kN–force capacity, fixed on the floor, and two other hydraulic oil jacks, similarly of 1000 kN–force capacity, fastened at the top of the transverse beam (Fig. 5(c)). All values of the applied force F were obtained from the sum of the measurements of two load cells, of 1000 kN–force capacity and 2 mV/V accuracy, located between the upper oil jacks and two steel plates (Fig. 5(c) and Table 2). This test condition was repeated three times for every point load F, resulting in a total of thirty–six tests. After the application of every load F, the prestress force $N_{0x,aver}$ always experienced a small increment, the values $N_{x,aver}$ as shown in Table 2.

Seven FBG–DSM sensors and seven LVDTs (labeled L0, …., L6) were positioned along the PCI beam's length at the cross sections i = 0, ..., 6, based on the test layout shown in Figs. 6 and

7(a). Steel plates were used to locate each sensor corresponding to the beam axis (Fig. 7(b)). Specifically, the reference FBG–DSM sensors and LVDTs (labeled r.p. and L0, L6 in Fig. 6) were located at the beam ends $i = 0$ and 6 to form a reference line for the measurement system between the boundary conditions. An additional LVDT was positioned on the opposite side of the midspan cross section $i = 3$ to measure possible rotations along the member axis. The LVDTs were connected to a data logger located on a desk close to the test rig. The FBG–DSM sensors were connected by optical wires along the PCI beam span and linked by a connecting pipe (Section "FBG–DSM system"). A static full spectrum optical interrogator positioned on the floor was used as the data logger to acquire the FBG–DSM signals.

Comparison between the measured displacements

The vertical displacements v_i for $i = 0, ..., 6$ (Fig. 6) were recorded by the FBG–DSM system and LVDTs after applying each vertical load F. The initial reference deflection shape corresponds to that after the assignment of prestress forces N_{0x1} and N_{0x2} (Fig. 6). Each prestress force $N_{x,aver}$ prevented the PCI beam from developing cracks under the load F. All test measurements were recorded every second for nearly 200 seconds by a data acquisition unit. The average measurements of the initial prestress forces (N_{0x2}, N_{0x1}, $N_{0x,aver}$), prestress forces (N_{x2}, N_{x1}, $N_{x,aver}$) when the loads F applied, loads F and deflections v_i for one repetition of the test combinations are listed in Table 2. Twelve test cases were defined, yielding a total of thirty–six tests (including the three repetitions). A good repeatability was experienced, in fact, errors lower than 2% were obtained between all reciprocal (repeated) measures. A mean relative error of 0.3% was obtained between the measured displacements v_1, v_3, and v_4. The displacement v_2 was characterized by a mean error of 0.1 mm and corresponding to a relative error of 1.5%. The displacement v_5 close to the end constraint was characterized by a mean error of 0.1 mm, leading a relative error of 1.3%. The mean relative and absolute errors of each measure v_i for $i = 1, ..., 5$ are reported at the bottom of Table 2.

In situ experiments

Bridge No. 24 of Highway No. 86 in Taiwan

The "2016 Southern Taiwan earthquake" occurred in the early morning of February 6th with epicenter in the Meinong District in Kaohsiung City. A moment magnitude of 6.4 was registered. The earthquake caused numerous collapses of residential buildings in Tainan City. Bridge No. 24 of Highway No. 86, at approximately 24 km far away from the epicenter (Fig. 8(a)), reported some damages after the earthquake. The superstructure of Bridge No. 24 consists of 4 units with a total length of 1,115 m. The "east" bound part has a length of 555 m, whereas the "west" bound part has a length of 560 m (Fig. 8(b)). Each unit is a 7–span double concrete box–girder (A2–RP13–RP12–RP11–RP10–RP9–RP8–RP7) with a single span of 40.0 m (Fig. 9). The width of each box–girder cross section is of 2.0 m. The substructure is a double concrete pier (Fig. 8(b)). One single pier cross section is of 1.5 m × 3.0 m, whereas the pier height varies in a range of approximately 4.5 ~ 7.0 m. After the "2016 Southern Taiwan earthquake", many bridge's supports were damaged. Specifically, one box–girder dislocated outwards from the original line at expansion joint labeled "RP7" (Fig. 8(b)). The dislocation measured up to 59 cm (Fig. 10(a)). NCREE commissioned a special inspection to be conducted on Bridge No. 24 in order to appraise its structural safety.

The monitoring system and related test layout

A short–term monitoring system based on *in situ* loading testing was planned by the Bridge Engineering Division of NCREE. The system was deployed along two spans of the dislocated box–girder and, specifically, between the supports labeled "RP9", "RP8" and "RP7" (Figs. 9 and 10(a)). The location of the devices is shown in Fig. 11 and described as follows:

Dial indicator: Nine dial indicators, of 0.01–mm tolerance, were positioned on the underside of the two span bridges at the cross sections i = 0, ..., 8 (Fig. 11). Scaffolding were used to fix each sensor onto stable platforms in correspondence of the beam axis (Fig. 10(b)). In detail, two reference dial indicators, labeled “D1” and “D2”, were placed at the pier support “RP8” at i = 1 and 2, whereas one reference dial indicator, labeled “D8”, was located at the beam end at i = 8. Thus, the system reference line between the boundary conditions was formed by the dial indicators at support “RP8” and the dial indicator at support “RP7”. All sensors were connected to a data logger positioned on the ground. Figure 11 depicts the dial indicator locations with red points.

FBG–DSM system: Nine FBG–DSM sensors with total length “S1+FBG+S2” of 100 mm (Fig. 1), maximum stroke of 40 mm, suspended cylindrical object of 60 mm–diameter and 0.1 mm–tolerance were employed (Fig. 10(c)). Similarly, the single–mode optical fiber with acrylic coating was used (Table 1). The FBG–DSM sensors were located inside the two box–girder spans at the cross sections i = 0, ..., 8 (Fig. 11), in correspondence of the bridge axis. Likewise, two reference FBG–DSM sensors, labeled “B” and “C”, were placed at the support “RP8” at i = 1 and 2, while one reference FBG–DSM sensor, labeled “I”, was positioned at the beam end at i = 8. Two additional FBG–DSMs, labeled “J” and “K”, were positioned on the opposite side of the midspan cross section at i = 5 to measure possible rotations along the span (Fig. 11). Therefore, the reference line for the system between the boundary conditions was formed by the FBG–DSMs at support “RP8” and the FBG–DSM at support “RP7”. The FBG–DSMs were linked by optical wires and by a connecting pipe (see Section “FBG–DSM system”). The FBG–DSM sensor, labeled “A”, was used for temperature compensation. A static full spectrum optical interrogator positioned on the ground was utilized as the data logger. Figure 11 shows the FBG–DSM sensor locations with yellow rectangles, vice versa, the connecting pipe is depicted with a red line.

Static loading tests

The span between the supports “RP8” and “RP7” of Bridge No. 24 was subjected to a series of static tests (Chiu et al. 2014, Sung et al. 2016). Four trucks were fully loaded, each with an approximate weight of 243 kN. Three test combinations (Tests 1, 2 and 3) were performed by single vehicle loading F of approximately 243, 729 and 486 kN at the midspan (Fig. 11). Additional four test combinations (Tests 4, 5, 6 and 7) were conversely performed by double vehicle loading $F_1 + F_2$ of approximately 243 + 243, 484 + 486 and 241 + 243 kN (Fig. 12(a)–(b)). Each truck loading F and $F_1 + F_2$ prevented the concrete box–girder from developing cracks. Numerical results based on the influence line were used to determine the load distribution. The truck number and positions of all seven test combinations are shown in Table 3. In Tests 4, 5, 6 and 7, the longitudinal distances from the support "RP8" were respectively of 14.25, 11.5 and 14.25 m, as illustrated in Fig. 12(a), which were calculated between the mass center of trucks. Notably, the loading tests were conducted after the bridge closure, subsequently to the "2016 Southern Taiwan earthquake".

Comparison between the measured displacements

The vertical displacements v_i for i = 0, ..., 8 were measured by the FBG–DSM system and dial indicators positioned at the same cross sections, after applying each truck loading F or $F_1 + F_2$ (Figs. 11 and 12). All displacements were recorded every second for nearly 15 minutes by a data acquisition unit. The average deflection measures v_i, for i = 3, 4, 5, 6 and 7, of the seven test combinations (Section 5.3) are listed in Table 3. Good agreement between the measurements from FBG–DSMs and dial indicators were obtained. A mean absolute error of 0.6 mm was achieved between the measured displacements v_3 and v_4. The displacement v_5 was characterized by a mean absolute error of 0.9 mm, vice versa, the displacement v_6 was characterized by a mean error of 0.4 mm. The displacement v_7 close to the span end furnished a mean error of 0.3 mm. Tests 5 and 7 reported higher errors because the dial indicator system (Section "The monitoring system and related test layout") did not consider the slight rotations along the bridge axis, in terms of displacement v_{rot} (Table 3), caused by the eccentric truck loading $F_1 + F_2$. The mean absolute errors of each measure v_i, for i = 3, 4, 5, 6 and 7, are reported at the bottom of Table 3. In general, such errors were probably caused by the thermal deformation of scaffolding, which affected each dial indicator measurement v_i (Fig. 10(b)). In all test combinations, no relaxation occurred in the FBGs inside the sensors and the tensile elongation along the fiber was considerably lower than its ultimate tensile elongation (Table 1). The effect of temperature variation on wavelength changes (sensor "A") was almost constant, therefore, wavelength changes in the FBG–DSMs were only caused by the span's vertical deflections. The comparison shown in Table 3 indicated that the displacement field of a bridge can be satisfactorily measured by the FBG–DSM system proposed in this study.

Conclusions

Static tests on a large–scale PCI beam and on Bridge No. 24 of Highway No. 86 in Taiwan were conducted for analyzing the performance of displacement measurements by the proposed FBG–DSM liquid–level system. A small range of second–order effects, i.e., lower than 4.5% of N_{crE}, was induced to prevent cracking phenomena along the PCI beam during testing. This study also enriches the limited testing by FBG–DSM system in the field. Thus, the following conclusions can be drawn:

- The obtained displacements using the FBG–DSM system matched properly with the corresponding experimental displacements using LVDTs, resulting in a mean error of 0.8%.
- The obtained *in situ* displacements by the FBG–DSM system matched properly with the corresponding displacements by dial indicators, resulting in a mean absolute error of 0.6 mm.
- The FBG–DSM sensing system has the high potential for short term measurements referring to an absolute reference and without any external physical reference to the ground.
- The FBG–DSM sensing system can substitute the manual geodetic technique required to survey the level of decks for routine bridge management.
- Dial indicators and LVDTs require fixed references below the measurement points. In fact, these sensors must be fixed onto a stable scaffolding in order to obtain accurate measurements, and the platform must be close to the span, which leads to increased cost and

difficulty associated with its construction. Scaffolding are subjected by thermal deformation that affects the displacement field and, moreover, they cannot be deployed for long term measurements.

- By contrast, FBG–DSMs can be located inside the girders of slab–on–girder and box–girder bridges without required any fixed ground reference points.

The proposed FBG–DSM sensing system will be implemented making the communicating vessels in stainless steel and creating a suitable pumping system to fill the water from the ground. Finally, bridge investigations involving static vehicle loading will be conducted to analyze the potential of the FBG–DSM system for long term monitoring.

Acknowledgments

Laboratory and *in situ* testing were conducted by the Bridge Engineering Division of NCREE and supported by funding from the National Applied Research Laboratories (NCREE–06105C1005). M.B. acknowledges the financial support provided by the Ministry of Science and Technology of Taiwan (MOST 105–2811–E–492–001). N.T. acknowledges the financial support of the "Research Program FAR 2018" provided by the University of Ferrara. A special gratitude is extended to the technicians of NCREE and students of National Taiwan University, who provided considerable assistance to the authors.

References

ACI 318–14 (2014). Building Code Requirements for Structural Concrete and Commentary. American Concrete Institute, Farmington Hills, MI.

Aldar A (Ed.) (2013). *Health assessment of engineered structures: bridges, buildings, and other infrastructures*. World Scientific Publishing.

Annual Book of ASTM Standards (2016) Section 4: Construction vol. 04.02. Concrete & aggregates. American Society for Testing & Materials.

Bonopera M, Chang KC, Chen CC, Lin TK and Tullini N (2018a). Compressive column load identification in steel space frames using second–order deflection–based methods. *International Journal of Structural Stability and Dynamics* 18(7) Article number 1850092.

Bonopera M, Chang KC, Chen CC, Lee ZK and Tullini N (2018b). Axial load detection in compressed steel beams using FBG–DSM sensors. *Smart Structures and Systems* 21(1):53–64.

Bonopera M, Chang KC, Chen CC, Lin TK and Tullini N (2018c). Bending tests for the structural safety assessment of space truss members. *International Journal of Space Structures*. https://doi.org/10.1177/0266351118804123.

Bonopera M, Chang KC, Chen CC, Sung YC and Tullini N (2018d). Feasibility study of prestress force prediction for concrete beams using second–order deflections. *International Journal of Structural Stability and Dynamics* 18(10) Article number 1850124.

Bonopera M, Chang KC, Chen CC, Sung YC and Tullini N (2018e). Prestress force effect on fundamental frequency and deflection shape of PCI beams. *Structural Engineering and Mechanics* 67(3):255–265.

Chang KC, Lee ZK and Chen CC (2012). Structural assessment of a repaired cable bridge damaged in 1999 Chi–Chi earthquake. *Proceedings of the International Symposium on Engineering Lessons Learned from the 2011 Great East Japan Earthquake*, March 1–4, Tokyo, Japan.

Chiu YT, Lin TK, Hung HH, Sung YC and Chang KC (2014). Integration of in–situ load experiments and numerical modeling in a long–term bridge monitoring system on a newly–constructed widened section of freeway in Taiwan. *Smart Structures and Systems* 13(6):1015–1039.

Consales M, Principe S, Iele A, Leone M, Zaraket H, Jomaa I, Cutolo A and Cusano A (2018). A fiber Bragg grating liquid level sensor based on the Archimedes' law of buoyancy. *Journal of Lightwave Technology* 36(20):4936–4941.

Dai Y, Sun Q, Wo J, Li X, Zhang M and Liu D (2012). Highly sensitive liquid–level sensor based on weak uniform fiber Bragg grating with narrow–bandwidth. *Optical Engineering* 51(4) 044401.

Guan S, Bridge JA, Li C and DeMello NJ (2019). Smart radar sensor network for bridge displacement monitoring. *Journal of Bridge Engineering* 24(1).

International Federation for Structural Concrete (2003). Monitoring and safety evaluation of existing concrete structures. FIB Bulletin No. 22, Lausanne, Switzerland.

Kim NS and Cho NS (2004). Estimating deflection of a simple beam model using fiber optic Bragg-grating sensors. *Experimental Mechanics* 44(4):433–439.

Kim YS, Sung HJ, Kim HW and Kim JM (2011). Monitoring of tension force and load transfer of ground anchor by using optical FBG sensors embedded tendon. *Smart Structures and Systems* 7(4):303–317.

Lai CC, Au HY, Liu MSY, Ho SL and Tam HY (2016). Development of level sensors based on fiber Bragg grating for railway track differential settlement measurement. *IEEE Sensors Journal* 16(16):6346–6350.

Lee JJ and Shinozuka M (2006). Real-time displacement measurement of a flexible bridge using digital image processing techniques. *Experimental Mechanics* 46(1):105–114.

Lee ZK (2013). Dazhi bridge safety monitoring demonstration project. *Proceedings of the 5th International Conference on Advances in Experimental Structural Engineering*, November 8–9, Taipei, Taiwan.

Lee ZK, Chen CC, Hung HH, Sung YC and Lee LS (2014). Loading tests and long–term monitoring on Wugu–Yangmei viaduct of Taiwan National Highway. *Proceedings of the 5th Asia Conference on Earthquake Engineering*, October 16–18, Taipei, Taiwan.

Marecos J (1978). The measurement of vertical displacements through water levelling method. *Materials and Structures* 11(5):361–370.

Ozdagli AI, Gomez JA and Moreu F (2017). Real-time reference-free displacement of railroad bridges during train-crossing events. *Journal of Bridge Engineering* 22(10).

Rodrigues C, Felix C, Lage A and Figueiras J (2010). Development of a long–term monitoring system based on FBG sensors applied to concrete bridges. *Engineering Structures* 32(8):1993–2002.

Rodrigues C, Felix C and Figueiras J (2011). Fiber–optic–based displacement transducer to measure bridge deflections. *Structural Health Monitoring* 10(2):147–156.

Skelton SB and Richardson JA (2006). A transducer for measuring tensile strains in concrete bridge girders. *Experimental Mechanics* 46(3):325–332.

Sung HJ, Do TM, Kim JM and Kim YS (2017). Long–term monitoring of ground anchor tensile forces by FBG sensors embedded tendon. *Smart Structures and Systems* 19(3):269–277.

Sung YC, Lin TK, Chiu YT, Chang KC, Chen KL and Chang CC (2016). A bridge safety monitoring system for prestressed composite box–girder bridges with corrugated steel webs based on in–situ loading experiments and a long–term monitoring database. *Engineering Structures* 126 571–585.

Tullini N, Rebecchi G and Laudiero F (2012). Bending tests to estimate the axial force in tie–rods. *Mechanics Research Communications* 44 57–64.

Tullini N (2013). Bending tests to estimate the axial force in slender beams with unknown boundary conditions. *Mechanics Research Communications* 53 15–23.

Vurpillot S, Krueger G, Benouaich D, Clément D and Inaudi D (1998). Vertical deflection of a pre–stressed concrete bridge obtained using deformation sensors and inclinometer measurements. *ACI Structural Journal* 95(5):518–526.

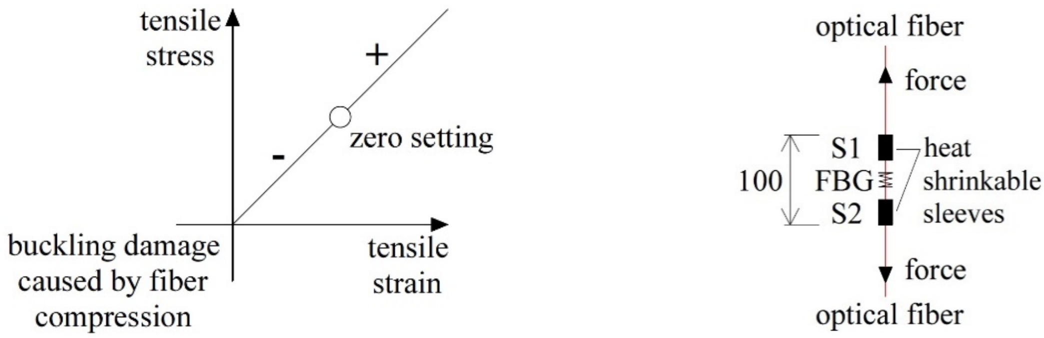

(a) **(b)**

Fig. 1. (a) Exerting prestress and setting sensing origin. (b) Connector introducing external force into the FBG (dimensions in mm).

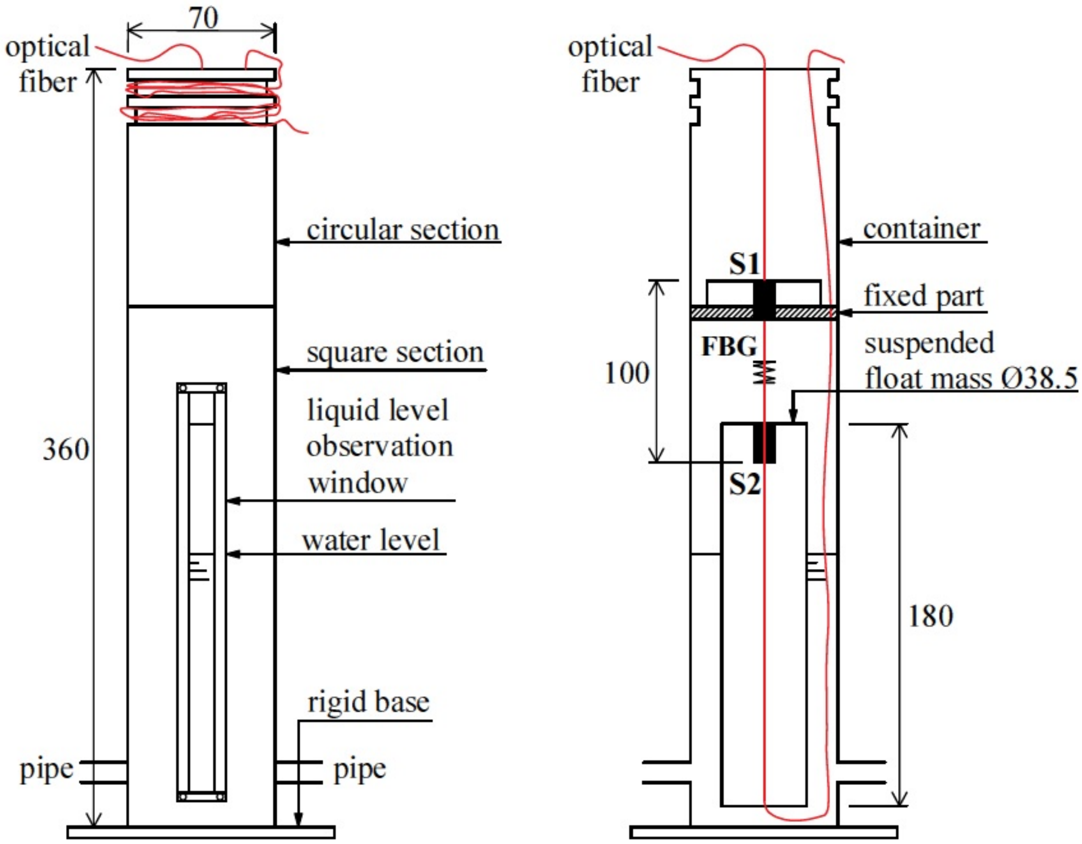

(a) **(b)**

Fig. 2. (a) External view and (b) internal system layout of the employed FBG–DSM sensor (dimensions in mm).

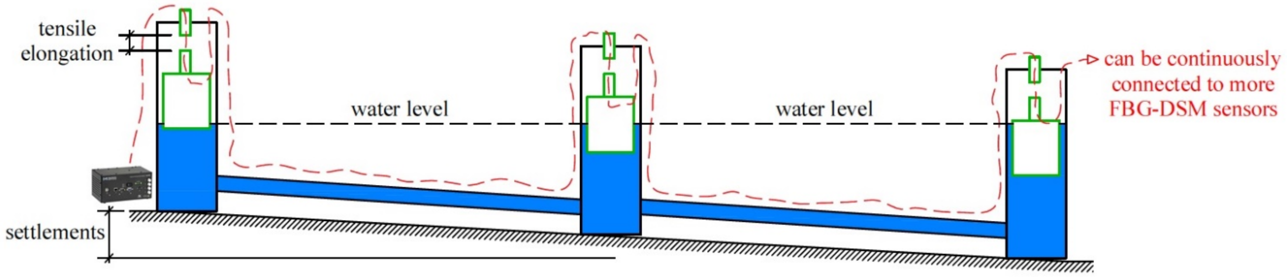

Fig. 3. Layout of the employed FBG–DSM sensing system.

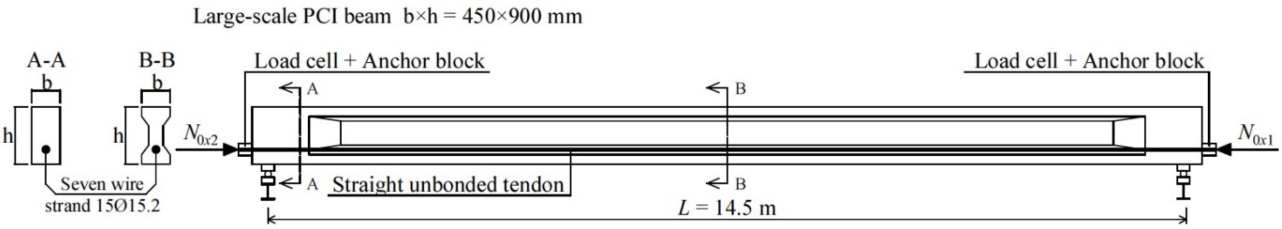

Fig. 4. Large–scale PCI beam with a straight unbonded tendon.

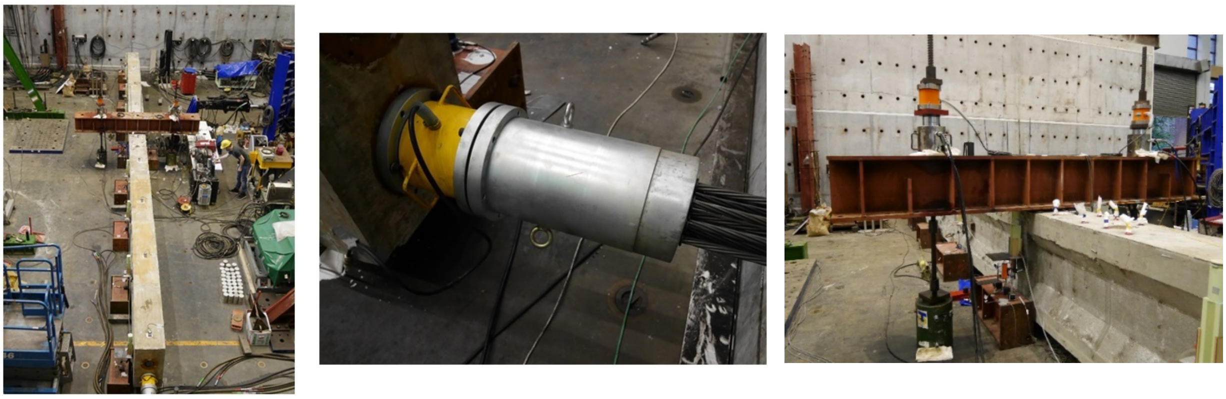

(a) **(b)** **(c)**

Fig. 5. (a) Indoor test rig. (b) Load cell at one PCI beam end. (c) Transverse steel beam at the PCI beam's midspan.

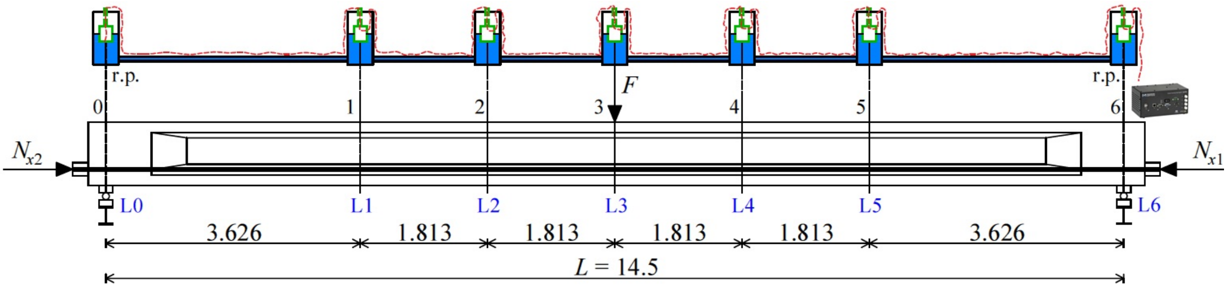

Fig. 6. Test layout with locations of instrumented sections with FBG–DSM sensing system (dimensions in m).

(a) FBG–DSM sensors and LVDTs along the PCI beam span.

(b) One FBG–DSM sensor on the steel plate.

(c) Reference FBG–DSM sensor and LVDT at one PCI beam end.

Fig. 7. Test layout of the employed FBG–DSM sensing system.

(a) **(b)**

Fig. 8. (a) Location of “2016 Southern Taiwan earthquake”. (b) Bridge No. 24 of Highway No. 86, Taiwan.

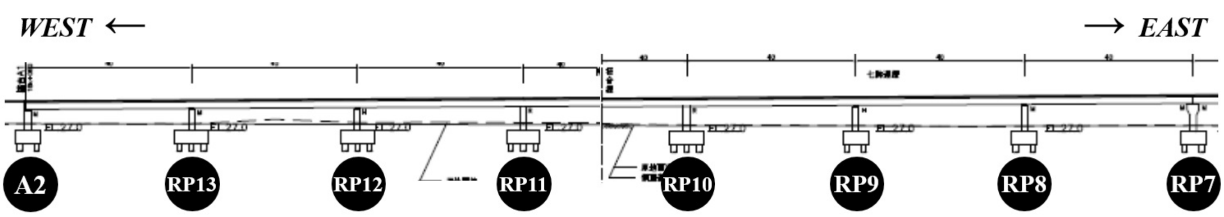

Fig. 9. One 7–span double concrete box–girder of Bridge No. 24.

(a) View before installation and detail of the dislocation at joint "RP7".

(b) One dial indicator fixed onto a stable platform.

(c) One FBG–DSM sensor inside the box–girder span.

Fig. 10. The short–term monitoring system.

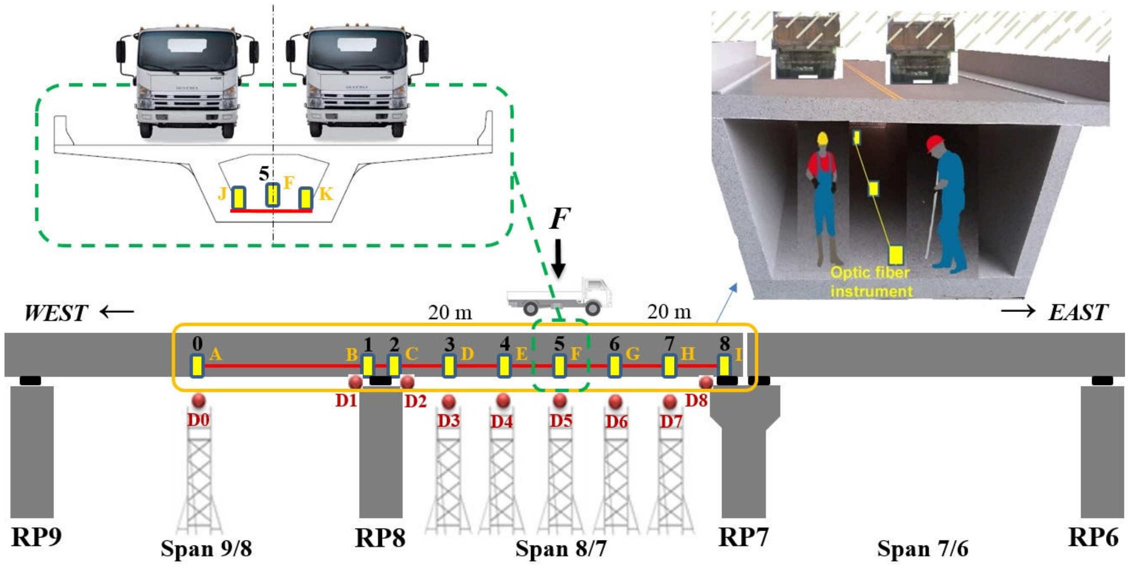

Fig. 11. Test layout with locations of instrumented sections with dial indicator and FBG–DSM sensing systems.

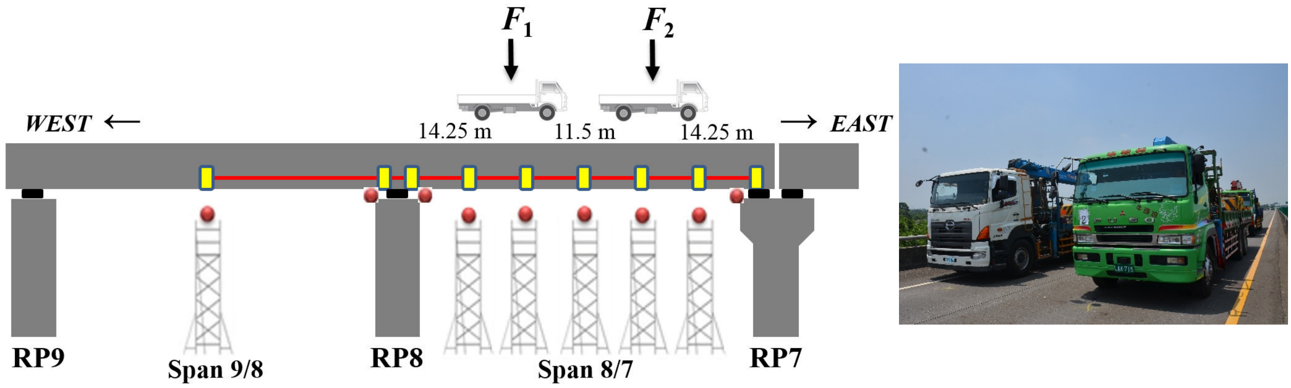

(a) (b)

Fig. 12. (a) Layout of Tests 4, 5, 6 and 7. (b) Double vehicle loading of Test 6 (484 + 486 kN).

Table 1. Main properties of the fiber in the employed FBG–DSM sensor.

Fiber type	single–mode optical fiber
Fiber coating	acrylate
Fiber grating length	15 mm
Fiber grating width spectral reflectivity	93.87%
Fiber center wavelength	1526.96 nm
Fiber strain optic coefficient	0.78 x 10^{-6}/με
Fiber tensile elongation (corresponding to the maximum stroke)	≈ 0.103 mm
Fiber ultimate tensile elongation	≈ 0.20 mm
Fiber wavelength shift (corresponding to the maximum stroke)	≈ 3.04 nm
Fiber wavelength shift (corresponding to its ultimate tensile elongation)	≈ 6 nm

Table 2. Comparison between the measured displacements v_i corresponding to the test layout depicted in Fig. 6.

Days of concrete curing	N_{0x2} [kN]	N_{0x1} [kN]	$N_{0x,aver}$ [kN]	N_{x2} [kN]	N_{x1} [kN]	$N_{x,aver}$ [kN]	F [kN]		v_1 [mm]	v_2 [mm]	v_3 [mm]	v_4 [mm]	v_5 [mm]
87	1514	1614	1564	1524	1620	1572	80.5	LVDT	3.68	4.85	5.29	4.80	3.59
								FBG–DSM	3.8	5.0	5.5	5.0	3.7
87	1514	1614	1564	1526	1622	1574	100.9	LVDT	4.58	6.08	6.67	6.03	4.47
								FBG–DSM	4.6	6.2	6.8	6.0	4.6
87	1520	1613	1567	1529	1624	1577	139.7	LVDT	6.26	8.35	9.21	8.34	6.25
								FBG–DSM	6.3	8.5	9.3	8.3	6.4
88	1668	1775	1722	1678	1789	1733	160.3	LVDT	7.29	9.64	10.56	9.60	7.37
								FBG–DSM	7.3	9.7	10.5	9.6	7.4
88	1668	1775	1722	1679	1790	1735	171.4	LVDT	7.85	10.40	11.42	10.36	7.93
								FBG–DSM	8.0	10.6	11.4	10.5	8.1
88	1668	1775	1722	1681	1792	1737	182.4	LVDT	8.43	11.20	12.31	11.14	8.51
								FBG–DSM	8.4	11.3	12.2	11.1	8.5
88	1754	1882	1818	1776	1896	1836	179.8	LVDT	8.13	10.77	11.84	10.73	8.18
								FBG–DSM	8.2	11.0	11.8	10.7	8.3
88	1764	1880	1822	1775	1895	1835	180.7	LVDT	8.16	10.81	11.86	10.79	8.24
								FBG–DSM	8.2	11.0	11.8	10.8	8.3
88	1754	1882	1818	1779	1898	1838	196.8	LVDT	9.06	12.05	13.30	12.00	9.10
								FBG–DSM	9.1	12.3	13.2	11.9	9.2
90	1848	1989	1918	1872	2002	1937	190.2	LVDT	8.52	11.26	12.37	11.18	8.51
								FBG–DSM	8.5	11.4	12.4	11.2	8.6
90	1859	1987	1923	1871	2002	1937	191.8	LVDT	8.68	11.48	12.55	11.44	8.77
								FBG–DSM	8.7	11.5	12.5	11.4	8.7
90	1848	1989	1918	1876	2006	1941	210.6	LVDT	9.64	12.80	14.10	12.71	9.61
								FBG–DSM	9.6	12.9	14.0	12.7	9.7
								Mean relative error [%]	**0.6**	**1.5**	**0.2**	**0.2**	**1.3**
								Mean absolute error [mm]	**0.0**	**0.1**	**0.1**	**0.1**	**0.1**

Table 3. Comparison between the measured displacements v_i corresponding to the test layout depicted in Figs. 11 and 12.

		F [kN]		v_3 [mm]	v_4 [mm]	v_5 [mm]	v_6 [mm]	v_7 [mm]	v_{rot} [mm]
Test 1	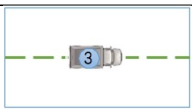	243	Dial indicator	1.0	1.9	2.4	2.0	1.2	–
			FBG–DSM	0.9	1.6	2.0	1.9	1.1	0.0
Test 2	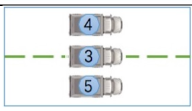	729	Dial indicator	3.5	5.9	7.6	6.4	4.0	–
			FBG–DSM	2.7	5.1	6.4	6.0	3.5	0.0
Test 3	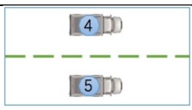	486	Dial indicator	2.5	4.2	5.3	–	2.8	–
			FBG–DSM	1.9	3.6	4.5	4.2	2.6	0.0
		$F_1 + F_2$ [kN]		v_3 [mm]	v_4 [mm]	v_5 [mm]	v_6 [mm]	v_7 [mm]	v_{rot} [mm]
Test 4	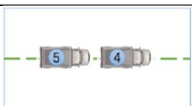	243 + 243	Dial indicator	2.2	3.6	4.6	–	2.5	–
			FBG–DSM	1.7	3.1	3.8	3.6	2.2	0.0
Test 5	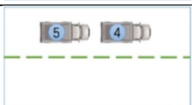	243 + 243	Dial indicator	2.2	3.7	4.6	–	2.6	–
			FBG–DSM	1.7	3.1	3.9	3.6	2.2	-0.2
Test 6	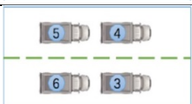	484 + 486	Dial indicator	4.4	7.1	9.0	7.6	4.9	–
			FBG–DSM	3.3	6.2	7.5	7.0	4.3	0.0
Test 7	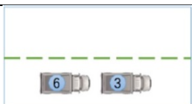	241 + 243	Dial indicator	2.3	3.8	4.7	–	2.6	–
			FBG–DSM	1.8	3.4	4.1	3.8	2.4	0.2
			Mean absolute error [mm]	**0.6**	**0.6**	**0.9**	**0.4**	**0.3**	**–**